Influence of silver seed layer thickness and zinc oxide concentration on p-type charge carriers in nanorods

S. K. Jubear[a], E. S. Hassan[b], O. M. Abdulmunem[b,*]
[a]*Ministery of Education, Directorate General for Education, Baghdad, Iraq*
[b]*Physics department, college of science, Mustansiriyah University, Baghdad, Iraq*

The hydrothermal technique (90°C, 6 h) was used in this study to generate negatively conductive zinc oxide (ZnO) nanorods (NRs) on silver (Ag) nucleation layers, which have been deposited on glass substrate through DC magnetron sputtering and had average thicknesses ranging from 150 nm to 1500 nm. The properties that were studied were optical, structural, and electrical. ZnO NR films were all polycrystalline, according to structural measurements, and (002) plane exhibited the dominant reflection. ZnO NRs' reflection intensity reduced as the thickness regarding Ag nucleation layer increased, suggesting a reduction in the crystallization intensity. Surface measurements demonstrated that there was a discernible change in the nanostructures' shape as the thickness of the Ag nucleation layer increased. The nanostructures went from radially spherical configurations to needles, irregular rods, and finally regular hexagonal rods perpendicular to glass substrate's surface. As the thickness of Ag nucleation layer rose, optical tests revealed a drop in transmittance and an increase in optical energy gap values, while Hall measurements revealed an increase in the concentration of hole charge carriers from 8.755 10^{17} cm^{-3} to 12.788 10^{17} cm^{-3}.

(Received June 30, 2024; Accepted September 5, 2024)

Keywords: Zinc oxide nanorods, vacuum thermal evaporation, p-type, Silver led seed layer, DC magnetron sputtering

1. Introduction

Zinc oxide (ZnO) is a versatile metal oxide material used in water purification, chemical sensors, piezoelectric devices, photocatalysis, gas sensors, UV photodetectors, photo-anodes, and energy harvesting systems because it can easily be formed into thin films, nanoparticles, nanowires, nanorods (NRs), and flower-like structures. Several methods have been used to prepare various ZnO NRs, such as chemical methods, ultrasonic irradiation [1], molecular beam epitaxy [2], thermal evaporation [3], RF sputtering [4], vapour-phase transport [5], and chemical vapour deposition [6]. However, the most common approach is the hydrothermal method [7–9], in which various nanostructures can be prepared by reacting Zn with catalysts.

Silver (Ag) is an excellent catalytic material for the growth of ZnO nanostructures, as it has chemical and physical properties that promote the formation of NRs in a controlled and efficient manner. It can lead to the enhancement of some physical characteristics of zinc NRs like their chemical resistance, flexibility, and thermal conductivity, leading to the expansion of their possible applications. Silver can be defined as a chemical element belonging to Group I in the periodic table with an atomic number of 47. It can be characterized by a group of significant chemicals and physical characteristics: it is of a high level of electric conductivity, easily mouldable and soft, and can be formed to a variety of shapes like silver paper, wire, and thin films. Those characteristics have made it a desirable material in the industry.

ZnO and silver characteristics may be used in combination; silver is known for its good electrical conductivity, while zinc oxide gives transparency and semi-conductivity. Which is why, the rod that can be yielded from the ZnO/Ag has high electrical characteristics from the silver in addition to its semi-conducting characteristics. Rods that are made of the ZnO/Ag can be used in a

* Corresponding author:: munem@uomustansiriyah.edu.iq
https://doi.org/10.15251/JOR.2024.205.589

wide range of things such as touch screens, and transparent electronic devices like flexible electronics and displays. ZnO/Ag rods, taking under consideration their good optical characteristics, can find use as well in the lighting applications as well as other optical devices such as lasers. Moreover, they could be employed to create photovoltaic devices such as solar cells, optical sensors, and various sophisticated systems like medical tools.

ZnO/Al thin films with varying weight ratios (0, 2, 4, and 6 wt%) were produced by Abdulmunem et al. [10] using a thermal evaporation technique, resulting in thin semiconducting films with negative electrical n-type conductivity. Regarding ZnO, the shift in Fermi level toward the conduction band level EF was determined to be 0.427 eV, while for ZnO/Al, it was 0.667 eV. In forbidden energy band, the secondary donor levels Ed have been determined to be 0.142 eV for ZnO/Al and 0.220 eV for ZnO. A 2wt% sample had a width of 10 nm and height of 200 nm in a 2D atomic force microscope image analysis of the emergence of nanowires along the x-axis. At 6wt%, the height increased to 240 nm.

Kayani et al. [11] altered the Ag/ZnO nanoparticles' structural, morphological, and optical characteristics using the sol-gel technique. They discovered that a combination of the sol-gel method and Ag doping may be used to control the nanoparticles' crystallinity, morphology, and optical characteristics. According to their research, a polycrystalline hexagonal wurtzite structure was revealed using X-ray diffraction (XRD), wherein the size of the crystallites decreased from 36.95 to 28.11 nm as the amount of Ag dopant increased. The morphology of the surface revealed nanoparticle aggregation. Ag-doped ZnO NPs appeared to exhibit a red shift in the band gap, decreasing from 3.48 to 2.91 eV, indicating potential uses in photocatalysis.

The hydrothermal approach was employed by Fang et al. [12] to synthesis p-doped ZnO NRs. The acceptor energy level generated by doped p atoms in the ZnO crystal lattice was confirmed by XRD and low-temperature photoluminescence spectra. The authors showed that the hydrothermal approach is a productive strategy to fabricate p-doped ZnO NRs by building a 1D ZnO nanostructure.

Ag thin film epitaxial template as well as dopant source for vertically aligned p-type ZnO NRs were investigated by Park et al. [13]. The Ag film was dissolved throughout the hydrothermal process to produce Ag^+ ions at a generate in the reaction solution. The (111) plane of Ag could serve as the epitaxial template for the (0001) plane of ZnO, and the Ag^+ ions could be employed to dope the wurtzite structure of ZnO. For use in electrical device applications, Ag-doped p-type ZnO NRs have been thus effectively grown on the substrate with n-type semiconductor. Using X-ray photoelectron spectra and XRD, Ag doping was effectively established. Through creating p-n diodes with Ag and Zn source depletion, the electrical p-type properties of Ag-doped ZnO NRs were proven.

2. Experimental

The process of growing ZnO NRs was carried out according to the following steps:

- Different thicknesses of Ag (Zhengzhou CY Scientific Instrument Co.) were deposited on glass substrate (2.5 × 7 cm) using a DC magnetron sputtering system. Table 1 shows the deposition times and the corresponding thicknesses of the seed layer, as well as the variables that were used during the deposition process.

Table 1. Shows the deposition times and the corresponding thicknesses of the seed layer.

Deposition time [s]	The Average correspond thickness [nm]	DC power [w]	Distance between target and substrate [cm]	Sputter pressure [torr]	Sputter gas
30	150	50	10	1×10^{-2}	Argon
60	200				
90	700				
120	1400				

- The substrate of Ag seed layers was annealed at 450°C for one hour.
- The development solution was prepared using 0.2, 0.5, 0.7, and 0.9 g of zinc nutria hydroxide ($Zn(NO_3)_2{\cdot}6H_2O$), 1 ml of ammonium hydroxide, and 30 ml of deionized water. All materials were mixed with a thermal magnetic mixer for 45 minutes at a temperature of 25°C.
- The Ag/glass substrate was placed in a 150 ml Teflon cell horizontally so that the precipitating face was facing down.
- The aqueous deposition solution was added to the Teflon cell so that the solution immersed all parts of the glass substrate.
- Teflon cell has been transferred to a stainless-steel autoclave and transferred to an electric oven, where it was left for 6 h at 90°C.
- The samples have been taken out following the specified time and left to cool naturally.
- The samples have been extracted as well as rinsed with deionized water, then annealed for one hour at a temperature of 450°C.

3. Result and desiccation

Figure 1 shows the deposited Ag seed layer produced in four different thicknesses (140, 250, 700, 1500 nm) according to four different deposition times (30, 60, 90, 120 s). On a glass substrate, the DC magnetron sputtering method was used for the deposition, and it was then annealed for one hour at 450°C. Figure 1 shows that the XRD pattern of all the prepared samples is polycrystalline and that the preferred reflections at the (111) level correspond to 2θ = 38.05°. The degree of crystallinity of this reflection increased with the deposition time (and thickness) due to the reduction of crystalline defects [14]. The Scherrer equation [15] was used to measure the crystallite size of the preferred reflection [16]:

$$D = \frac{k\lambda}{\beta\ cos\theta} \tag{1}$$

It can also be seen from Figure 1 that there are four secondary reflections at the levels (222), (311), (220), and (200), corresponding to the reflection angels 2θ = 44.31°, 64.34°, 77.34°, and 81.63°. All reflections in Figure 1 are compatible with the JCPDS Data File No. 04-0783 [16]. The microstrain and dislocation density measurement process was carried out by applying the following equations [17][18]:

$$\varepsilon = \frac{1}{D^2} \tag{2}$$

$$\delta = \frac{\beta}{4\tan\theta} \tag{3}$$

Both the microstrain and dislocation density decrease with increasing thickness of the Ag seed layer. Table 2 lists the measured as well as calculated values from the XRD measurement.

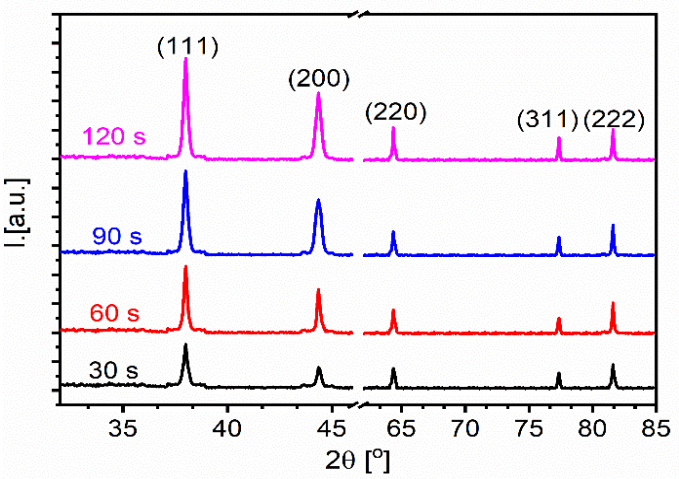

Fig. 1. X-ray diffraction of the silver seed layer deposited by DC magnetron sputtering.

Table 2. Includes the XRD measuring and calculated values.

Thickness [nm]	2θ [°]	(hkl)	Lattice Parameter [nm]	Crystallite size [nm]	Micro strain $\times 10^{-4}$	Dislocation density$\times 10^{14}$ [1/m^2]
140	38.01	(111)	4.086	29.50	18.390	82.8028
250	38.01	(111)	4.086	34.75	15.6119	77.9636
700	38.01	(111)	4.086	35.81	15.1488	60.0638
1500	38.01	(111)	4.086	40.80	13.2965	11.48974

Figure 2 shows field emission scanning electron microscopy (FESEM) top and cross-section images of the Ag seed layer, with different thicknesses deposited using a DC magnetron sputtering technique on the glass substrate and annealed at 450°C for 1 h. In Figures 2a and a1, it can be seen that the surface of the sample deposited at 30 s is slightly rough and homogeneous, and the particle size is within the limits 20–15 nm. As for the cross section, the thickness of the layer is in the range 184–147 nm. Figures 2b and b1 represent the growth seed layer at a time of 60 s. The particle size grows by about 20–30 nm and that large particles are scattered across the surface, covering approximately 20% [19]. As for Figure 2b1, which shows the cross section, the width of the deposited layer is about 250 nm. Figures 2c and c1, which show images of the development layer at a time of 90 s, reveal that the number of spherical-shaped particles has increased and that they cover a larger area of about 90% of the surface. As for the width of the development layer, we note that it has increased to about 700 nm due to the increase in deposition time [20]. Figures 2d and d1 show the growth layer at time 120 s. The particles deposited on the surface have attained a regular spherical shape due to the gathering of smaller particles into the form of a large spherical particle. They are spread on the surface in an almost regular manner and have become larger, at around 300 nm. The thickness of the layer has increased to approximately 1500 nm due to the increase in deposition time [21].

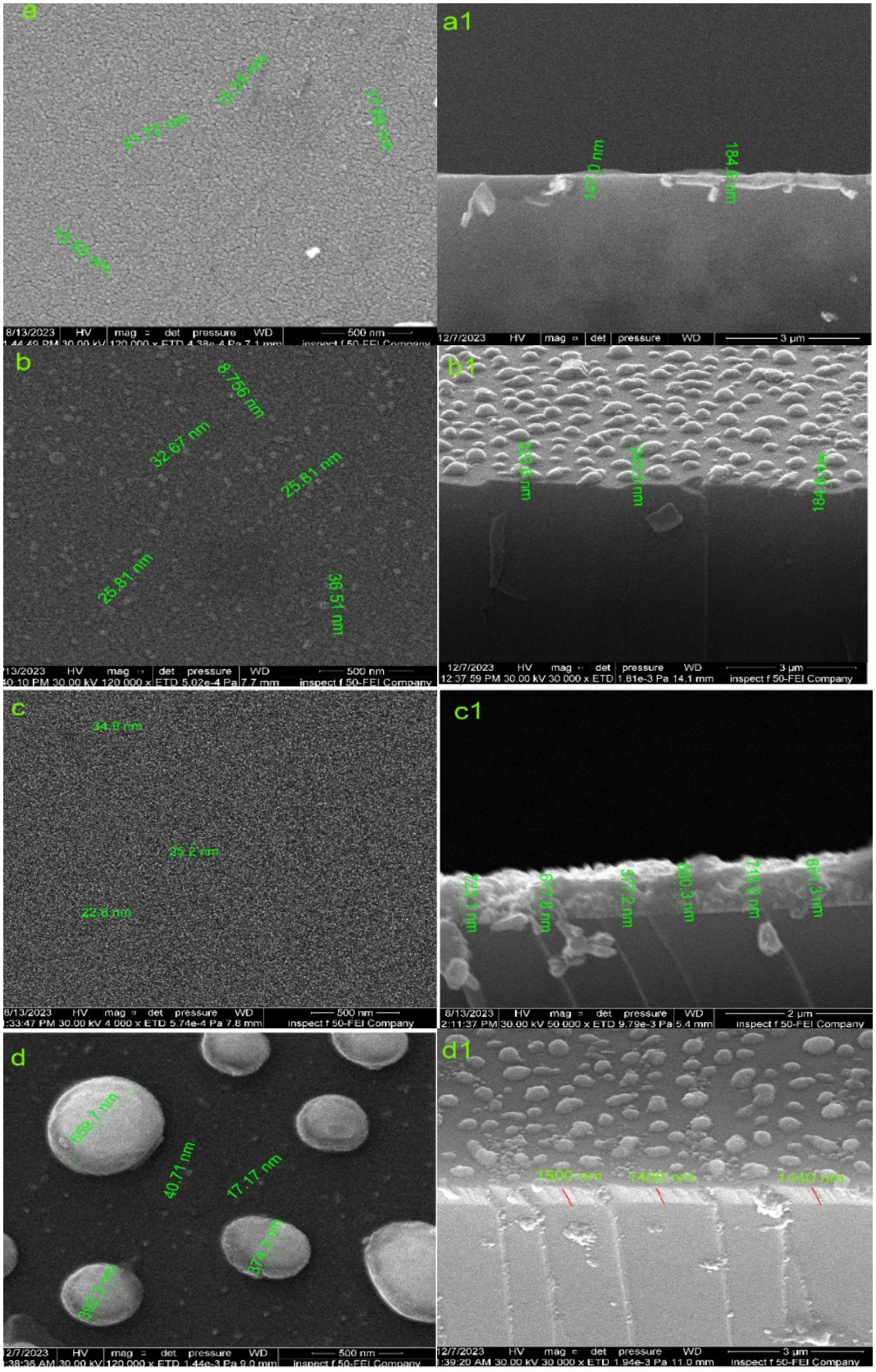

Fig. 2. FESEM of silver seed layer deposited by DC sputter (a and a1) 60 sec., (b and b1) 90sec., (c and c1)120 sec., and (d and d1) 150 sec top and cross section view respectively.

Figure 3 shows the transmittance spectra of Ag seed layer samples deposited on a glass substrate, with different deposition times, using a DC magnetron sputter technique. It can be observed from the transmittance spectrum as a function of wavelength that the transmittance decreases from 87.29% to 78.86% with increasing deposition time (the thickness of the deposition seed layer increases from 140 nm to 1500 nm, due to the increase in both the crystallite size and the scattering sites [22]). It is also apparent that the transmittance spectrum falls in the region of wavelengths from 350 to 1000 nm.

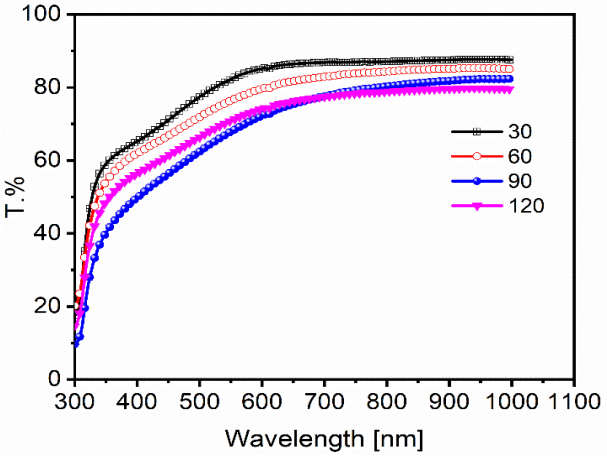

Fig. 3 Transmittance as function to the wavelength of silver seed layer deposited by DC magnetron sputtering.

Figure 4 shows the XRD spectrum of ZnO/Ag NRs. All the models with different thicknesses (140, 400, 700, and 1500 nm) have a polycrystalline diffraction pattern and the dominant reflection is from the (002) plane at the angle $2\theta = 34.49°$ in the pure wurtzite phase of ZnO with a hexagonal structure (JCPDS database card number 36-1451). In contrast, in the fcc Ag seed layer, the dominant reflection is in the (111) plane at the angle $2\theta = 38.05°$. It can also be seen that the intensity of the dominant reflection from the (002) plane decreases as the deposition time of the Ag seed layer increases. This is because of the Ag-occupied substitution sites and the difference in the ionic diameters of Ag^{+} (0.126 nm) and Zn^{2+} (0.074 nm) [23]. This may be associated with moderate degradation loss of the periodicity of the crystal lattice, resulting in excess Ag incorporation [24]. The crystallite size, microstrain, and dislocation density were calculated by applying equations (1), (2) and (3), and the following equations [25] were used to calculate the lattice parameters *a* and *c*:

$$a = \frac{\lambda}{(3)^{1/3}\, sin\theta_{(002)}} \tag{4}$$

$$c = \frac{\lambda}{sin\theta_{(002)}} \tag{5}$$

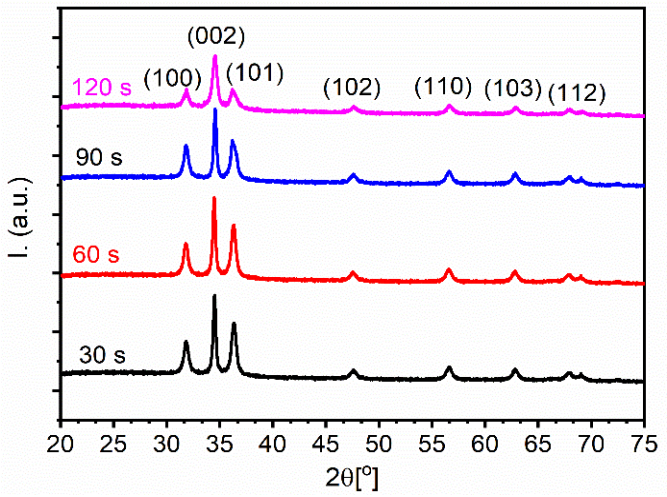

Fig. 4. X-ray diffraction of the ZnO NRs/ Ag seed layer deposited by DC magnetron sputtering.

Table 3 lists some values measured with XRD and calculated from the equations. In addition to the primary reflection at (002), there is a group of secondary reflections at (100), (101), (102), (110), (103), and (112) corresponding to angles 2θ = 31.81°, 36.25°, 47.57°, 56.57°, 62.88°, and 68.02°.

Table 3. Includes some values measured and calculated from X-ray diffraction measurements.

Thickness [nm]	2θ [°]	(hkl)	Lattice Parameter a and c [nm]	Crystallite size [nm]	Macrostrain $\times 10^{-4}$	Dislocation density$\times 10^{14}$ [1/m^2]
140	34.59	(002)	3.249-5.206	21.57	22.571	21.474
250	34.59	(002)	3.249-5.206	22.82	21.341	19.197
700	34.59	(002)	3.249-5.206	21.17	23.002	22.301
1500	34.59	(002)	3.249-5.206	16.92	28.783	34.920

Figure 5 shows FESEM images of ZnO NR samples of thickness 140 nm, which were prepared using hydrolysis. It can be seen from Figures 5a, a1, and a2 that nanostructures formed by ZnO are hexagonal rods, with bases larger than their tops (i.e. a conical shape), and with NRs connected to their bases in the form of concentric star structures. Further, the structures have different lengths and diameters, with the average length being 2.825 µm and the average diameter at the base and top being 340 and 225 nm, respectively. Figures 5b, b1, and b2 show FESEM images of ZnO NRs samples with a thickness of 400 nm. It can be seen from the figure that the star structures disappear and are replaced with individual rod-like structures that are not connected within the Ag base texture. The lengths of these rods range between 1000 and 1250 nm and they are spread irregularly due to the increase in thickness and thus to the increase in Ag^+ ions [26]. Figures 5c, c1, and c2 show FESEM images of ZnO NR samples of 700 nm, revealing that the rod-like nanostructures disappear and are replaced with nanostructures in the form of bundles of rods that are irregular in shape but have a homogeneous surface. The average diameters of these nanostructures are 70 nm at the peaks. The choice of precursor seeds and growth conditions can determine the final morphology of the ZnO nanostructures. For example, the length and diameter of ZnO NRs are influenced by the precursor seeds used in the growth process [27]. Figures 5d, d1, and d2 show FESEM images depicting the growth of ZnO NR samples in the form of a regular hexagonal shape with vertical growth on the surface. The diameter of the hexagonal rods at the top is around

60 nm. The morphology of the nanostructured seed layer plays a key role in the growth of vertical ZnO NRs, with the seed layer showing ZnO nanocrystal clusters with a hexagonal shape [28].

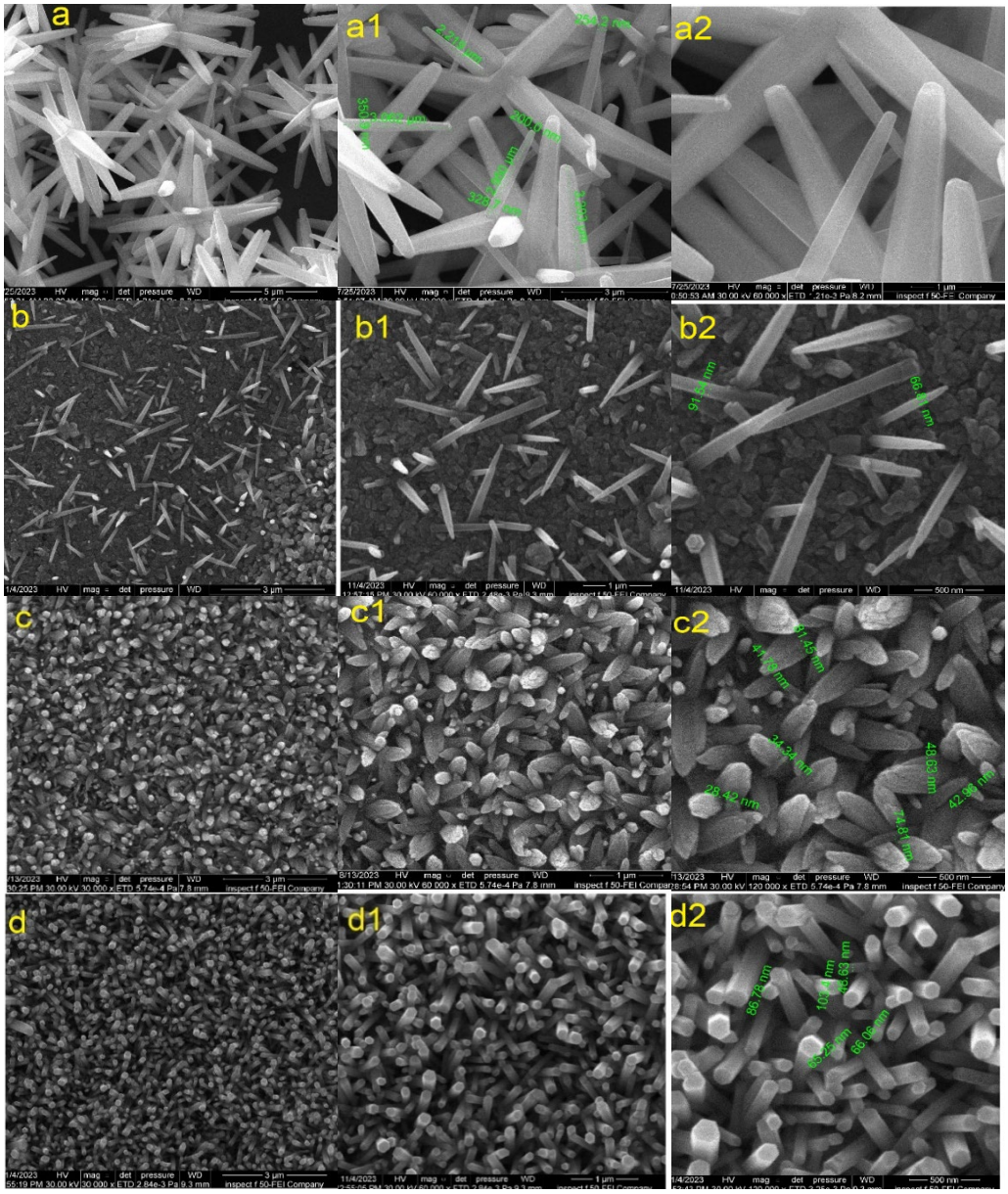

Fig. 5. SEM of silver seed layer deposited by DC sputter (a, a1 and a2) 60 sec., (b, b1 and b2) 90sec., (c, c1 and c2)120 sec., and (d, d1 and d2) 150 sec (top view).

Figure 6 shows the transmittance spectrum of ZnO NR samples prepared using the hydrolysis method with different thicknesses of Ag seed layer (140, 400, 700 and 1500 nm). It can be seen from Figure 6 that the transmittance spectrum is equal for the first two thicknesses (140, 400 nm) because of the strong similarity between the nanostructures growing on Ag surfaces, as is evident in Figure 5. The transmittance spectra for the models with thickness 700 and 1500 nm have lower amplitudes than the first two because increasing the thickness leads to a decrease in crystallinity and grain size [29]. It is also apparent from the figure that the transmittance region is located at the wavelengths 800–200 nm, that is, in the ultraviolet and visible regions. The energy gap values were calculated from the following equation [30]:

$$(\alpha h\vartheta)^2 = B(E_g - h\vartheta)^2 \quad (6)$$

where hv is the photon energy, α is the absorption coefficient, B is a constant, and E_g is the energy band gap.

Figure 7 shows that the energy gap values increase with the thickness of the Ag layer. This is due to the decrease in the degree of crystallization with increasing thickness (decreasing grain size), which reduces the mobility of the charge carriers [31].

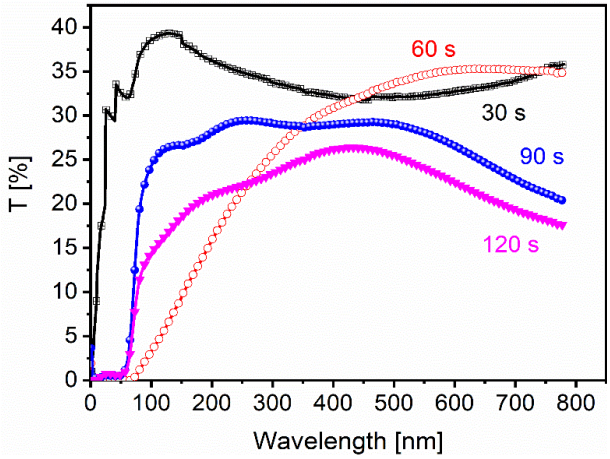

Fig. 6. Transmittance as function to the wavelength of ZnO NRs/Ag seed layer deposited by DC magnetron sputtering.

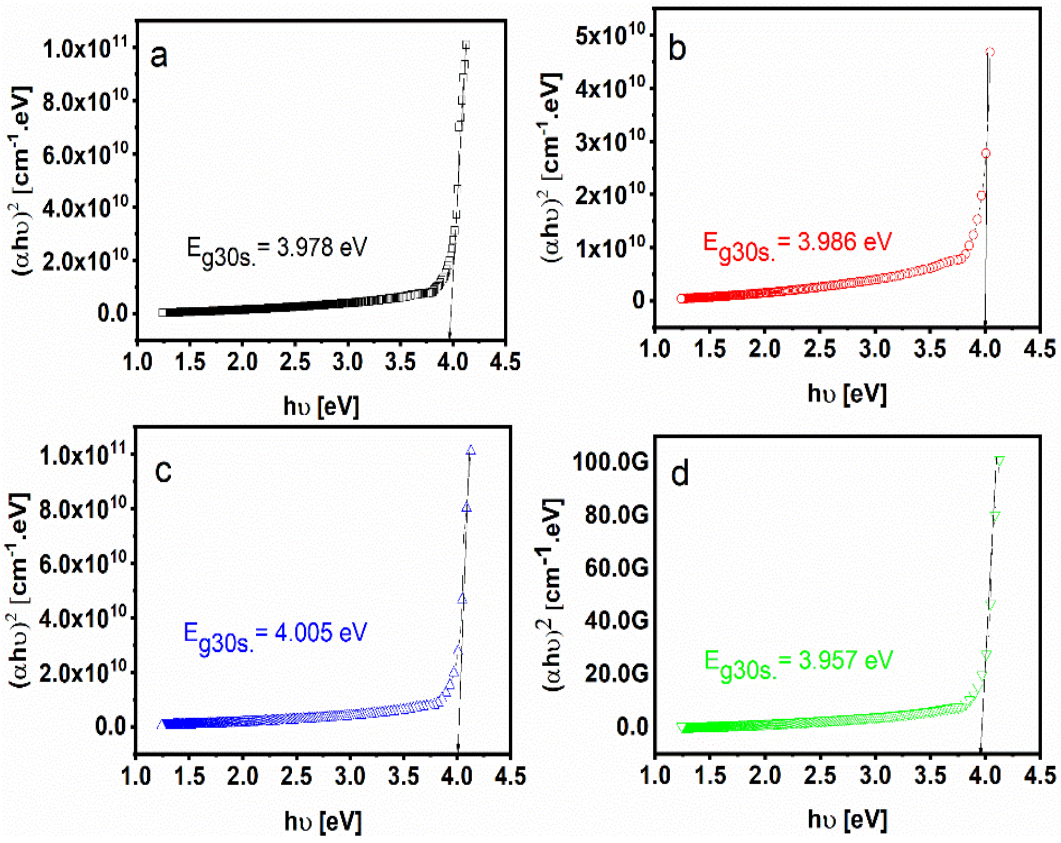

Fig. 7. Energy band gap values extrapolating from $(\alpha h\upsilon)^2$ as function to $(h\upsilon)$ of ZnO NRs/Ag seed layer deposited by DC magnetron sputter(a)140nm, (b) 400 nm, (c) 700 nm and (d) 1500 nm.

The electrical properties were obtained through Hall measurement, yielding values for the charge carrier concentration, electrical resistivity, and Hall mobility for different thicknesses of Ag (150, 200, 700, and 100 nm), which are associated with different deposition times (30, 60, 90, and 120 s). Figure 8 shows that the electrical resistivity decreases from 12 × 10^{-2} Ω cm to 10.5 10^{-2} Ω cm as the thickness of the nucleation layer of Ag increases from 150 nm to 1500 nm. This is due to the change in resistivity, the Ag^{+} ions acting as acceptor sites in the energy gap acceptor levels in the ZnO crystal, and the Ag^{+} ions having higher valence levels and a larger ionic diameter than the host material ZnO so that the Ag will occupy alternative sites in the host material and thus the number of holes increases [32]. The concentration of hole charge carriers increases with the thickness of the Ag seed layer, due to the increase in concentration of vacancies in the ZnO texture [33]. It is also apparent from the figure that the mobility decreases slightly with an increase in the thickness of the Ag seed layer. This is because of the reduction in crystallization with increasing Ag concentration [31].

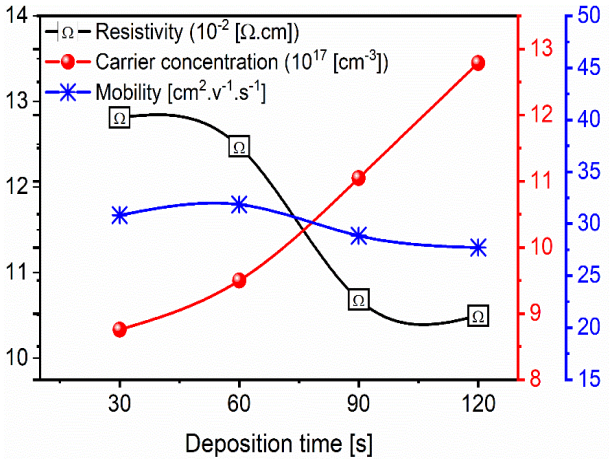

Fig. 8. Hall measurement resistivity, carrier concentration, and mobility of ZnO NRs/Ag seed layer deposited by DC magnetron sputtering.

4. Conclusions

All the prepared samples (Ag and ZnO NRs) have a polycrystalline diffraction pattern. The crystallite size increases with the thickness of the Ag seed layer. The crystallite size decreases as the thickness increases in the growth of ZnO NRs. The particle size and the homogeneity of semicircular nanostructures both increase in the Ag seed layer. ZnO NRs appear with different shapes, namely radial spherical structures, needles, irregular rods, and finally regular hexagonal rods perpendicular to the surface of the glass substrate. The transmittance decreases for all models (Ag seed layer and ZnO NRs). Negative conductivity (p-type) appears with an increase in the concentration of charge carriers from the holes with increasing thickness of the growth layer.

Acknowledgements

The authors would like to express their gratitude and acknowledge the department of physics staff at the college of science of the Mustansiriyah University, the Laboratory of Advanced Materials, for making the necessary measurements.

References

[1] R. Rayathulhan, B.K. Sodipo, A.A. Aziz, Ultrasonics sonochemistry, 35, 270-275, (2017); https://doi.org/10.1016/j.ultsonch.2016.10.002
[2] B. Nikoobakht, C.A. Michaels, S.J. Stranick, M.D. Vaudin, Applied Physics Letters, 85(15), 3244-3246, (2004); https://doi.org/10.1063/1.1803951
[3] J.H. Zheng, Q. Jiang, J.S. Lian, Applied Surface Science, 257(11), 5083-5087, (2011); https://doi.org/10.1016/j.apsusc.2011.01.025
[4] H.S. Al-Salman, M.J. Abdullah, Journal of alloys and compounds, 547, 132-137, (2013); https://doi.org/10.1016/j.jallcom.2012.08.119
[5] A.C. Mofor, A.S.Bakin, A. Elshaer, D. Fuhrmann, F. Bertram, A. Hangleiter, J. Christen, A. Waag, Physics A. 88, 17-20, (2007); https://doi.org/10.1134/S0036023624600680
[6] O.M. Abdulmunem, E.S. Hassan, J Opt (2024); https://doi.org/10.1007/s12596-024-01943-6
[7] H. A. Hameed, Al-Mustansiriyah Journal of Science, 29(3), 158–167, (2019); https://doi.org/10.23851/mjs. v29i3.636
[8] S.K. Jubear, O.M. Abdulmunem, E.S. Hassan, Digest Journal of Nanomaterials & Biostructures (DJNB), 19(1), (2024); https://doi.org/10.15251/DJNB.2024.191.
[9] S.A.H. Abbasa, Hassanb, E.S., O.M. Abdulmunemb, Digest Journal of Nanomaterials & Biostructures (DJNB), 18(3), (2023); https://doi.org/10.21123/bsj.2023.8336.
[10] O.M. Abdulmunem, M. J. Mohammed Ali, E. S. Hassan, Optical Materials 109, 110374, (2020); https://doi.org/10.1016/j.optmat.2020.110374.
[11] Z. N. Kayani, F.Manzoor, A. Zafar, M. Mahmood, M. Rasheed, M. Anwar, Optical and Quantum Electronics, 52, 344, (2020); https://doi.org/10.1007/s11082-020-02460-z.
[12] X. Fang, J. Li, D. Zhao, D. Shen, B. Li, X. Wang, The Journal of Physical Chemistry C. 113(50), 21208-21212, (2009); https://doi.org/10.1021/jp906175x.
[13] J. Park, T.I. Lee, J.M. Myoung, International Journal of Materials and Metallurgical Engineering, 9(1), 114-117, (2015)
[14] H.M. Mikhlif, M.O. Dawood, O.M. Abdulmunem, M.K. Mejbel, Acta Physica Polonica: A., 140(4), (2021); https://doi.org/10.12693/APhysPolA.140.320.
[15] K.G. Mohammed, I.R. Agool, F.S. Abdulameer, M.O. Dawood, O.M. Abdulmunem, N.F. Habubi, S.S. Chiad, IOP Conference Series: Earth and Environmental Science, 790 (1), 012080, (2021); https://doi.org/10.1088/1755-1315/790/1/012080.
[16] T. Holland, A.M. Abdul-Munaim, C. Mandrell, R. Karunanithy, D.G. Watson, P. Sivakumar, Lubricants, 9(4), 37, (2021); https://doi.org/10.3390/lubricants9040037.
[17] M. J. Mohammed, Al-Mustansiriyah Journal of Science, 32(3), 33–41, (2021); https://doi.org/10.23851/mjs.v32i3.944.
[18] E.S. Hassan, O.M. Abdulmunem, Brazilian Journal of Physics, 52(5), 160, (2022); https://doi.org/10.1007/s13538-022-01158-9.
[19] O. Pryshchepa, P. Pomastowski, B. Buszewsk, Advances in Colloid and Interface Science, 284, 102246, (2020); https://doi.org/10.1016/j.cis.2020.102246.
[20] H. Liu, B. Wang, E.S. Leong, P. Yang, Y. Zong, G. Si, J.Teng, S.A. Maier, ACS nano., 4(6), 3139-3146, (2010); https://doi.org/10.1021/nn100466p.
[21] X. Zhao, C.S.Wang, N.N. Chou, F.H. Wang, C.F. Yang, Materials, 16(7), 2647, (2023); https://doi.org/10.3390/ma16072647.
[22] C. Zhang, J. Zhao, H. Wu, S. Yu, Journal of Alloys and Compounds, 832, 154983, (2020); https://doi.org/10.1016/j.jallcom.2020.154983.
[23] Ö.A.Yıldırım, H.E. Unalan, C. Durucan, Journal of the American Ceramic Society, 96(3), 766-773, (2013); https://doi.org/10.1111/jace.12218.
[24] Z.N. Kayani, F. Manzoor, A. Zafar, M. Mahmood, M. Rasheed, M. Anwar, Optical and Quantum Electronics, 52, 1-18, (2020); https://doi.org/10.1007/s11082-020-02460-z.
[25] N. Iwashita, C.R. Park, H. Fujimoto, M. Shiraishi, M. Inagaki, Carbon, 42(4), 701-714, (2004); https://doi.org/10.1016/j.carbon.2004.02.008.
[26] C. Damm, H. Münstedt, Applied Physics A. 91, 479-486, (2008); https://doi.org/10.1007/s00339-008-4434-1.

[27] S. Del Gobbo, J. Poolwong, V. D'Elia, Crystal Growth & Design, 19(11), 6792-6800, (2019); https://doi.org/10.1021/acs.cgd.9b01226.
[28] A.P. Dharani, A.S. Amalraj, S.C. Joycee, V. Sivakumar, G. Senguttuvan, International Journal of Nanoscience, 19(02), 1950005, (2020); https://doi.org/10.1142/S0219581X19500054.
[29] N. Bahadur, A.K. Srivastava, S.Kumar, M. Deepa, B.Nag, Thin Solid Films, 518(18), 5257-5264, (2010); https://doi.org/10.1016/j.tsf.2010.04.113.
[30] N.F. Habubi, O.M. Abdulmunem, Z.M. Shaban, I.R. Agool, M.O. Dawood, S.S.Chiad, IOP Conference Series: Earth and Environmental Science, 790(1), 012078, (2021); https://doi.org/10.1088/1755-1315/790/1/012078.
[31] M. Öztas, M. Bedir, Thin Solid Films, 516(8), 1703-1709, (2008); https://doi.org/10.1016/j.tsf.2007.05.018.
[32] M. Farooq, S. Shujah, K.Tahir, S. Nazir, A.U. Khan, Z.M.Almarhoon, V. Jevtovic, H.S. Al-Shehri, S.T. Hussain, A. Ullah, Inorganic Chemistry Communications, 136, 109189, (2022) ; https://doi.org/10.1016/j.inoche.2021.109189.
[33] S.M. Mishra, B. Satpati, Journal of Luminescence, 246, 118813, (2022); https://doi.org/10.1016/j.jlumin.2022.118813.